Journal of Physics and Chemistry of Solids 148 (2021) 109669

Contents lists available at ScienceDirect

Journal of Physics and Chemistry of Solids

journal homepage: http://www.elsevier.com/locate/jpcs

Defects and grain boundary effects in MoS_2: A molecular dynamics study

Zahabul Islam, Aman Haque *

Department of Mechanical Engineering, The Pennsylvania State University, University Park, PA, 16802, USA

ARTICLE INFO

Keywords:
Mechanical properties
Grain boundaries
Polycrystalline
Molecular dynamics
Hall-petch

ABSTRACT

Mechanical properties of low-temperature large area chemical vapor deposited (CVD) transition metal dichalcogenides such as MoS_2 are a function of crystallinity, which tends to deteriorate with the presence of grain boundaries (GBs) and defects. In this study, we report mechanical properties of polycrystalline as well as single crystal MoS_2 containing defects and dopant atoms. To investigate mechanical properties we adopted computational approach using classical molecular dynamics (MD) simulation. Our calculated mechanical properties such as tensile strength, Young's modulus of single-crystal MoS_2 are in good agreement with the existing literature and alter with the appearance of GBs and defects. Polycrystalline MoS_2 samples exhibit GB strengthening i.e., Hall-Petch effects. A detailed investigation of a specific type of GB tilted sample also shows GBs insensitive fracture behavior. A small amount of sulfur vacancy and oxygen doping (<2%) exhibit ductility in the sample at the expense of failure strength. We also notice local plastic deformation which yields ductility in the sample. Our present study shows the detailed mechanism behind the plastic deformation behavior of single as well as polycrystalline sample.

1. Introduction

Transition metal dichalcogenide crystal (TMDCs) such as molybdenum sulfide (MoS_2) in two-dimensional (2D) form has attracted tremendous interest among the scientific community because of their distinctive electrical [1–5], optical [6,7], catalytic [8,9] and mechanical [10–13] properties. TMDCs materials has been widely used to fabricate transistors [14–16], sensors [17–19] and flexible electronics [20,21]. Among other 2D TMDCs, MoS_2 is the most widely studied material, and it has three phases namely 2H, 1T and 1T' phase. Among these three phases, 2H–MoS_2 configuration is more common and semiconducting [22,23] in nature, whereas 1T-MoS_2 is metallic [22,24–26]. Both top-down [27,28] and bottom-up [29–31] techniques are widely used for the synthesis of 2H–MoS_2. It is well known that both of these fabrication techniques yield defects such as grain boundaries, vacancy defects, ring defects, etc. [32–35]. These defects and grain boundaries in MoS_2 tend to deteriorate physical properties.

Defects and disorder play dominant role in physical properties of nanomaterials. For example, defect-free graphene and carbon nanotube (CNTs) has superior mechanical properties, however the inclusion of defects such as vacancy, different types of ring defects deteriorate its mechanical properties [36–38]. Similar to graphene and CNTs, pristine monolayer MoS_2 processes higher mechanical strength and superior electrical properties compared to their polycrystalline counterpart and defective MoS_2 [12,39]. Though the mechanical properties are well known for graphene [40–42] and to some extent for single crystal MoS_2 [10,43–45]; however, mechanical properties of polycrystalline as well as defective and doped 2H–MoS_2 remain largely unknown. Additionally, unlike graphene MoS_2 has ABAB type stacking i.e., S_{top}-Mo-S_{bottom} which might also exhibit a different deformation dynamics during mechanical straining [46,47]. It is well known that defects in TMDCs such as MoS_2 are inevitable and frequently developed during the synthesis. Thus it is crucial to understand their effects on physical properties. For example, brittleness in MoS_2 due to the hydrogenation has been reported recently [39]. Effects of grain boundaries on mechanical properties of MoS_2 using virtual nanoindentation has been also studied recently [33]. Despite a significant amount of effort has been put to investigate mechanical properties of MoS_2, specific types of defects and their concentration, distribution remains unexplored.

It is well known that oxidation might take place readily in 2H–MoS_2 under ambient conditions [48,49]. Alongside oxidation, chemical functionalization and doping are another viable routes towards modulation of the physical properties of MoS_2. For example, recent first principle calculation shows that oxygen doping might affect electronic, optical and magnetic properties [7,50,51]. Other studies [52,53] show that due to the large surface area and active ion adsorption sites MoS_2

* Corresponding author.
E-mail address: mah37@psu.edu (A. Haque).

https://doi.org/10.1016/j.jpcs.2020.109669
Received 25 April 2020; Received in revised form 13 July 2020; Accepted 16 July 2020
Available online 6 August 2020

could be a promising alternative for hydrogen evolution reaction (HER) compared to the precious platinum-based noble metal catalyst. However, previous studies reported inertness of the basal plane of 2H–MoS_2 for HER [54]. Both doping and vacancy introduction can overcome this issue by offering more active sites for ion adsorption and transport [55,56]. It has been reported that oxygen doping can be a viable solution to this problem, and can be achieved by treating with oxygen plasma which readily increases the number of active sites for HER [57]. Though doping atoms might enhance HER by introducing more active sites, their effects on mechanical properties are entirely remains unknown.

Due to the advancement in scanning/transmission electron microscopy (S/TEM) a significant amount of effort has been put to identify defects and GBs in 2D materials [40,58–60]. Additionally, few experimental studies [10,61] reported mechanical properties of monolayer MoS_2. However, exact deformation mechanisms have not been elucidated by the experiments. Thus in our present study, we take the resorts of atomistic simulations to investigate grain size, GBs, and defects such as vacancy and oxygen doping effects on the mechanical performance of the single crystal as well as polycrystalline 2H–MoS_2. We adopt a reactive forcefield based computational approach using classical molecular dynamics (MD) simulation implemented in the LAMMPS [62] simulation package. In the following sections, we will investigate mechanical properties of monolayer single as well as polycrystalline 2H–MoS_2 subjected to unidirectional tensile loading using molecular dynamics simulations to explore their deformation behavior and failure mechanisms.

2. Methods

In a classical MD simulation force field is used to define the potential energy of a system, which subsequently is used to calculate the atomic forces using Newtonian equation. Thus the choice of an appropriate forcefield is the key to successful MD simulations. Forcefield could be either reactive or non-reactive in-nature and they are derived based on experimental results or ab-initio (first principle) calculations. In our present study, we used ReaxFF [45] which is reactive in nature and its system energy terms could be expressed as follows:

$$E_{system} = E_{bond} + E_{over} + E_{under} + E_{val} + E_{pen} + E_{tor} + E_{conj} + E_{vdWaals} + E_{Coulomb} \quad (1)$$

The details of the ReaxFF can be found elsewhere [45]. Initially, we build 10 nm^2 single-crystal MoS_2 sheet to study the mechanical properties. To investigate mechanical properties of the polycrystalline MoS_2, we choose approximately 3 nm, 4 nm, 6 nm, 8 nm, 10 nm and 15 nm grain size oriented at 0°, 30°, and 60° as shown in Fig. 1b and marked by G1, G2 and G3 respectively. Before the tensile loading energy minimization molecular mechanics using conjugate gradient method was performed on both single and polycrystalline MoS_2 to obtain a minimum potential energy conformation. Such energy minimization was performed for all configurations. Next, molecular dynamics runs were executed using NPT ensemble with a time step of 0.25fs for several thousand steps at 1 atmospheric pressure and 300 K to achieve initial stress-free samples before the tensile loading. In our present study $2 \times 10^8\ s^{-1}$ strain rate was used during the tensile loading. All molecular dynamics simulations were performed using open-source LAMMPS [62] simulation package at room temperature i.e., 300 K.

To determine the mechanical properties, MoS_2 sheets were strained in both armchair (X-direction in Fig. 1a) and zigzag directions (Y-direction in Fig. 1a) and the internal stress of the cell was monitored. At the atomic level, stress can be defined in the form of virial stress as follows:

$$\sigma = -\frac{1}{V}\sum_{\alpha}\left(M^{\alpha}v_i^{\alpha}v_j^{\alpha} + \frac{1}{2}\sum_{\beta\neq\alpha}F_i^{\alpha\beta}r_j^{\alpha\beta}\right) \quad (2)$$

where the first term is associated with the contribution from kinetic energy due to thermal vibration and the second term is related to change in potential energy due to applied deformation. Here, V is the volume of the simulation cell and $V = \sum_{\alpha} V^{\alpha}$, V^{α} is the atomic volume of α; v_i^{α} and v_j^{α} is the i-component and j-component of the velocity of atom α. $F_i^{\alpha\beta}$ is the i-component of the force between atom α and β and $r_j^{\alpha\beta}$ is the j-component of the separation distance between atoms α and β [63].

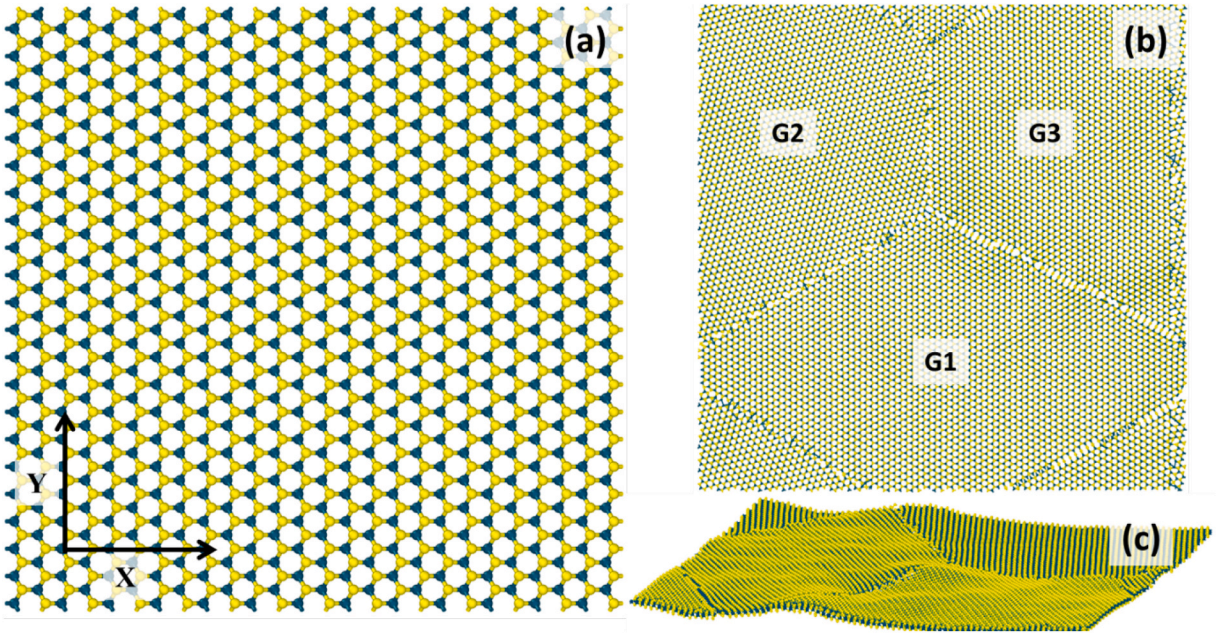

Fig. 1. MD simulation model of MoS2 (a) Single crystal, and (b) Polycrystalline sample with 15 nm grain size (Deep green and yellow color indicates Molybdenum and Sulfur atoms respectively), and (c) perspective view showing rippling in polycrystalline MoS2.

3. Results and discussions

3.1. Tensile response of monolayer MoS_2

In our present study, we investigate tensile response of monolayer 2H–MoS_2 in the armchair (X-direction in Fig. 1a) and zigzag directions (Y-direction in Fig. 1a) at 300 K temperature using ReaxFF forcefield. Recently, mechanical properties of MoS_2 have been studied using density functional theory (DFT) [64], experiments [10] and reactive potentials such as reactive empirical bond-order (REBO) [12,44,64] and ReaxFF [39,65]. The results such as Young's modulus and tensile failure strain obtained from all of these studies are in good agreement. Unlike graphene, MoS_2 has an ABAB type stacking sequence i.e S_{top}-Mo-S_{bottom} as shown in Fig. 2c. Each S atom in MoS_2 has 3-fold symmetry. This unique structure plays an important role in the deformation mechanism of MoS_2. Stress-strain plot in Fig. 2h exhibits three distinct regions. Initially, the curve follows Hook's law prior to the first Yielding. Afterward, the curve goes through the serration region, and finally, a drop in the stress-strain curve indicates failure in MoS_2. Simulation results as shown in Fig. 2h indicates that loading along armchair direction yields ultimate tensile strength approximately 24.5 GPa at a tensile strain of 27%. Calculated Young's modulus is 232 GPa which is in good agreement with both experimental [10] and computational [33,45] results. Our calculation shows first yielding occurs at 5.7% strain and corresponding Yield strength is 12.9 GPa. Serration in the stress-strain plot can be explained from the local plastic deformation as observed during the deformation (Fig. 2a–g). A similar type of plastic deformation occurs in stainless-steel and known as Lüder's band. To investigate the detailed deformation mechanism, we track shear strain on individual atoms as shown in Fig. 2a–g. We have noticed an onset of local plastic deformation at the first Yield point i.e 5.7% strain. As we increase tensile strain this local plastic deformation propagates perpendicular to the loading direction i.e along the zigzag edge as shown in Fig. 2b, and forms a deformation band (Please see the video

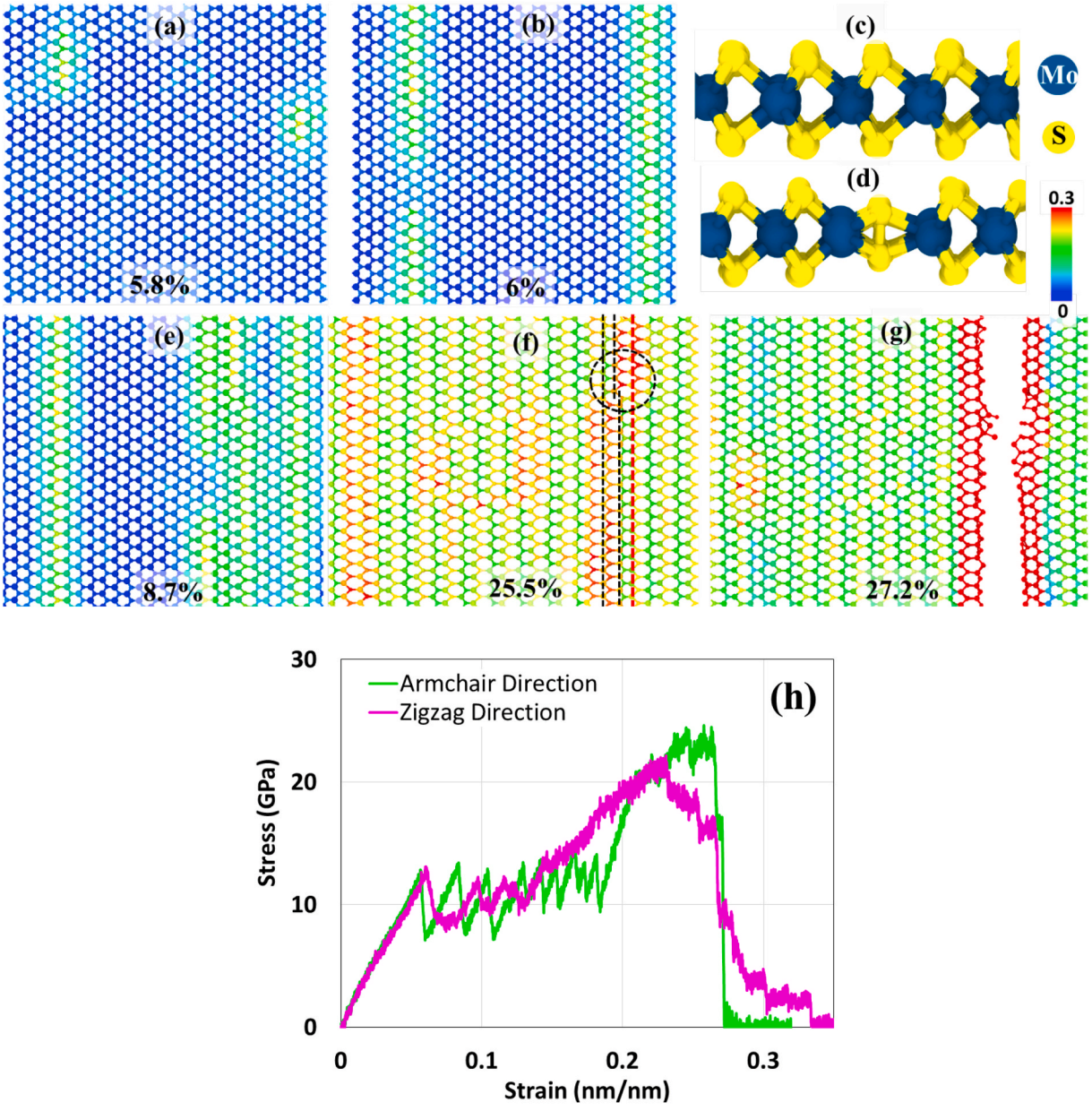

Fig. 2. Deformation behavior of 2H–MoS_2 under uniaxial loading at 300 K temperature: (a)–(g) shear strain mapping on Pristine sample, and (h) Tensile response of 2H–MoS_2.

1). These local deformation bands (Fig. 2e) in the MoS_2 are responsible for the serrated stress-strain behavior as we have observed in Fig. 2h. During this entire period of serration, we do not observe any significant amount of stress increment. However, once the serration period is over i.e the entire structure full of local plastic deformation band, tensile stress starts to increase until failure takes place as shown in Fig. 2f and g. During this local plastic deformation, S–S atoms move towards each other and form a bond which is shown in Fig. 2d. Mo atom in MoS_2 has six co-ordination and unlike Mo atoms S atoms has 3 co-ordination and thus they are assumed to have more mobility compared to Mo atoms. The formation of S–S bond is irreversible [45] i.e., after removal of load they cannot return to their initial position. Local stress concentration in the MoS_2 sample is shown in Fig. 2f prior to the failure. Dark dotted color line in Fig. 2f indicates Mo atomic layer perpendicular to the loading direction. However, at 25.5% tensile strain we notice a discontinuity in the Mo atomic plane. Top part of the Mo atomic layer has larger strain compared to the lower part which leads to the crack initiation in the sample and eventually sample fails at 27% tensile strain as shown in Fig. 2g. The crack path follows the zigzag edge of the MoS_2 sample. As we change the loading direction from armchair to zigzag both stress-strain pattern and deformation behaviors change. Fig. 3 shows the deformation mechanism during the tensile loading along the zigzag direction.

Unlike armchair deformation behavior, loading in the zigzag direction yields local plastic deformation band at an angle as shown in Fig. 3a. We have distinguished this plastic deformation band using shear strain distribution on each atom as shown in Fig. 3. The onset of local plastic deformation starts at an angle of 60° as shown in Fig. 3a. Upon the complete formation of a local deformation band, a new plastic deformation band forms along the zigzag edge as shown in Fig. 3b. Due to this local plastic deformation, we notice a drop in tensile stress as shown in Fig. 2h. As we continue to increase tensile strain a new deformation band with S–S bond forms as indicated by Fig. 3b and c. As mentioned earlier these local plastic deformation bands are responsible for the serration in stress-strain plot, and at higher strain stress concentration along the zigzag edge of the sample is observed (Fig. 3e and f). Failure initiate at 24.6% strain by forming a void at the same location where the first plastic deformation occurred (Fig. 3a and f). With further increment in the tensile strain, crack propagates along the zigzag edge of the sample as shown in Fig. 3g. It could be concluded that irrespective of loading direction crack propagates along the zigzag direction which supports the previous studies [12,59].

3.2. Effect defects and doping on mechanical properties of MoS_2

3.2.1. Sulfur vacancy effects on mechanical properties of MoS_2

It is well known that defects such as vacancy and doping might significantly affect the mechanical properties of MoS_2 [12,33]. Thus to assess the effect of vacancy defects on mechanical properties of MoS_2 we build molecular models with randomly distributed S vacancy (V_s) defects. In our present study, we randomly deleted 0.6% and 1.3% S atoms as shown in Fig. 4b. The red color circle indicates the deleted S atoms. Tensile response along the armchair direction is shown in Fig. 4a. It is evident that with the increment of the defects concentration both first Yield strength and strain reduces significantly. Calculated first Yield stress and strain for pristine MoS_2 are 12.9 GPa and 5.7% respectively. However, this yield stress value reduces by 21% and 32% for 0.6% and 1.3% S vacancy enriched samples respectively. Yield strain also shows a

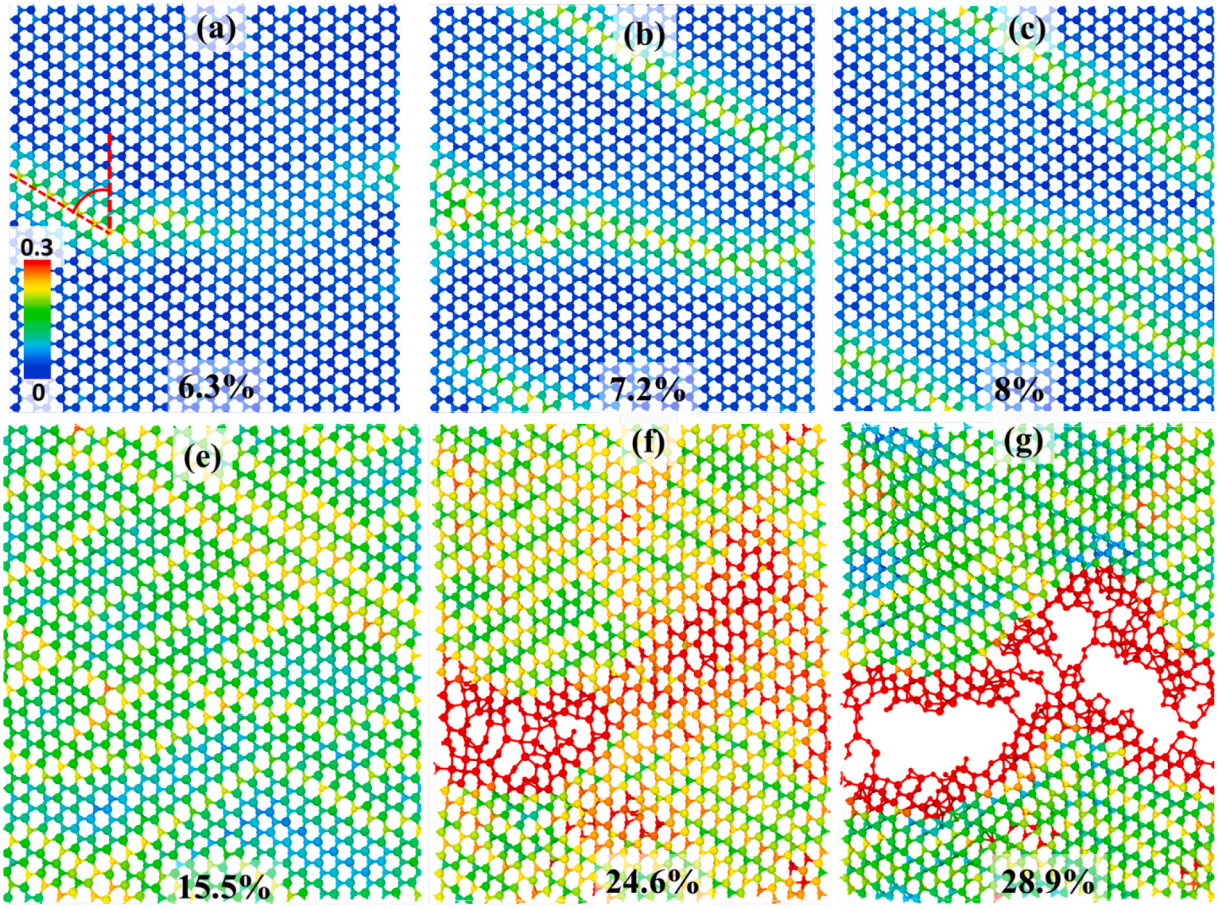

Fig. 3. Deformation behavior of 2H–MoS_2 under the tensile loading along the zigzag direction at 300 K temperature (scale bar indicates the magnitude of shear strain in the sample).

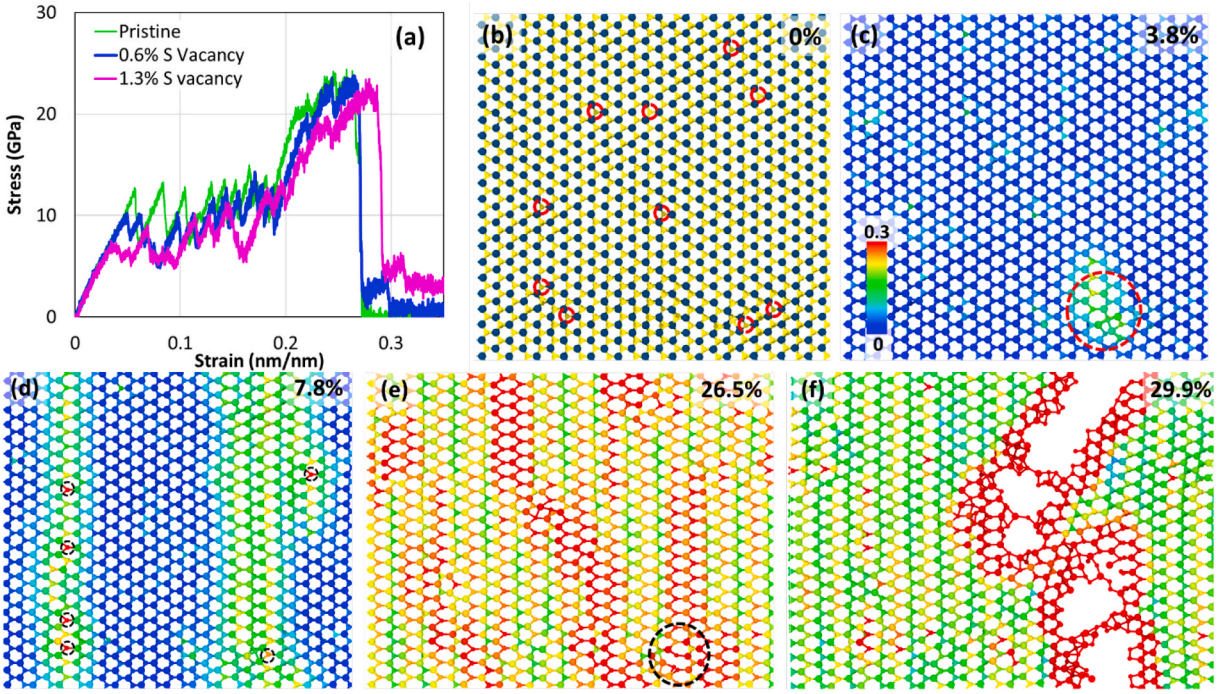

Fig. 4. Effect of sulfur (S) vacancy defects on mechanical properties of single crystal MoS_2 at 300 K temperature.

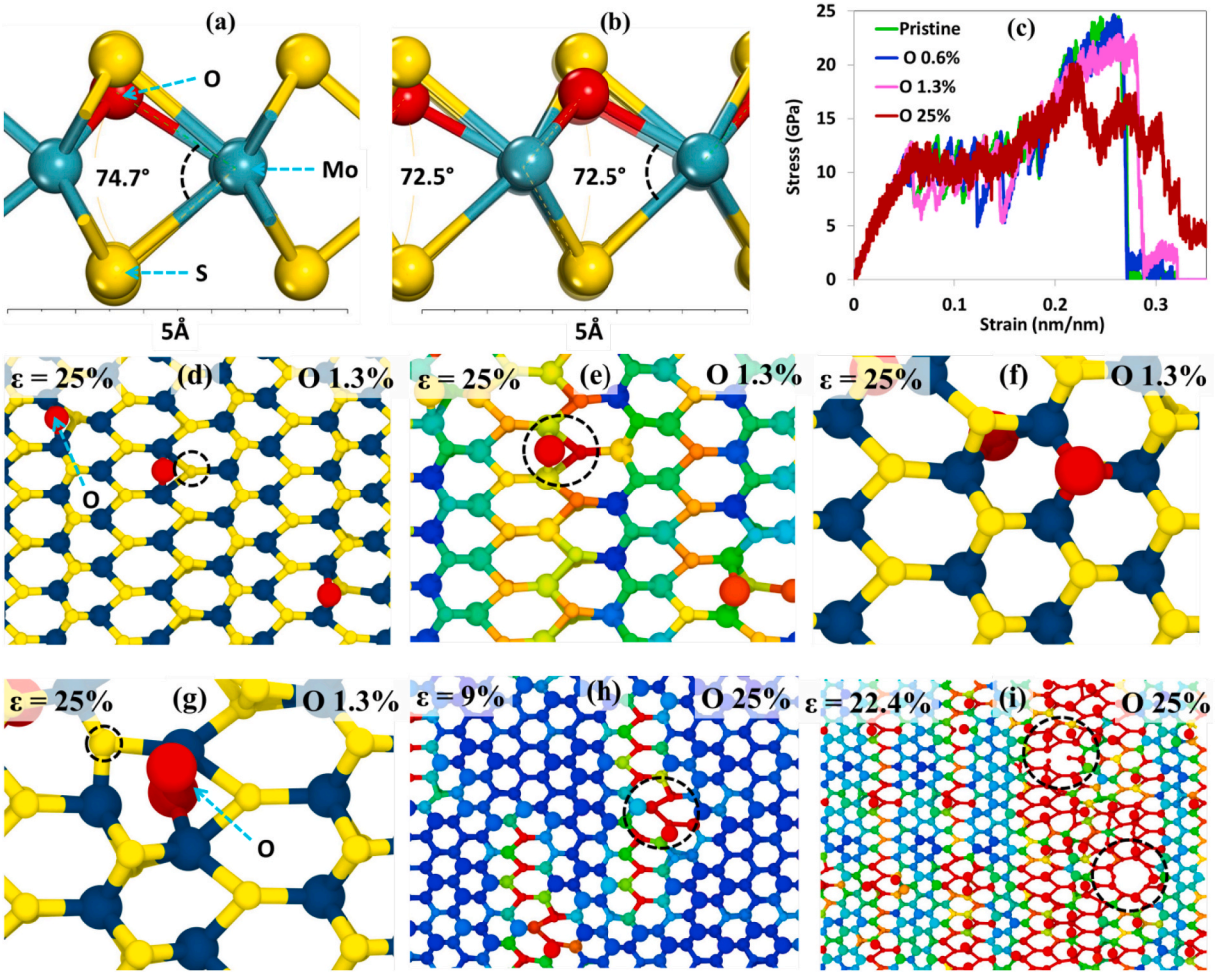

Fig. 5. O–Mo–S bond angle obtained from: (a) DFT study, (b) ReaxFF, and (c) Tensile response of O-doped MoS_2, and (d)–(i) virtual vacancy formation due to the O atom doping during tensile loading.

similar pattern and reduces by 15% and 26% respectively for 0.6% and 1.3% S deficient samples. Interestingly we notice that failure strain for 1.3% vacancy enriched sample is slightly higher than the pristine sample as evident in Fig. 4a. A similar type of vacancy enhanced ductility has been also observed in thin films [66,67]. To explain our observation we analyze MD simulation trajectory as shown in Fig. 4c–f. In these figures, atoms are colored by shear strain on the scale of 0–0.3. We notice amplified local deformation at the location of the vacancy enriched area as shown by the dotted red color circle in Fig. 4c. Very similar to the pristine structure this local deformation extends to form a band and gradually saturates the entire sample. This amplified strain at the location of V_s will develop stress concentration around it as shown by the dotted dark color circle in Fig. 4d. Though shear strain remains almost constant along with the deformation band, S vacancy enriched area has higher shear strain compared to the defect-free region. This local higher strain may contribute to the enhancement of overall failure strain. A comparison between Fig. 4c and e indicate the failure initiates from the same location where the first stress concentration occurred as marked by a dark color dotted circle in Fig. 4e. At this location bond rotation and new ring-type defects such as 4|8 ring forms prior to the failure (Fig. 4e). It is worth mentioning that GBs with 4|8 ring defect has lower energy compared to 4|6 and 6|8 GB defects [33]. Additionally, 4|8 ring defect is associated with higher elastic deformation energy due to the larger Burger vector [68]. These factors might facilitate the formation of 4|8 ring defect at higher strain. However, above failure strain, we notice crack deflection and crack propagation along the zigzag edge as shown in Fig. 4f.

3.2.2. *Oxygen doping effects on mechanical properties of MoS_2*

In this section, we have assessed the effect of oxygen (O) doping on the mechanical performance of the single crystal MoS_2 as shown in Fig. 5. Prior to the MD simulations, we optimize O-doped 2H–MoS_2 structure using ReaxFF and plane-wave based density functional theory (DFT). DFT calculation was performed using CASTEP [69] code considering generalized gradient approximation (GGA) and Perdew-Burke-Ernzerhof (PBE) function for electron exchange-correlation. Ultrasoft pseudopotentials were implemented for electron-ion interaction and a convergence criterion of 10^{-6} eV/atom with an energy cut-off 340eV was set. Our calculated optimized S–Mo–O bond angle using DFT (Fig. 5a) and ReaxFF (Fig. 5b) is 74.7° and 72.5° respectively which is in good agreement with recent DFT study [7], and comparatively smaller than the pristine S–Mo–S bond angle which is found to be 80.66° [7]. Reduction in bond angle indicates compression of O atoms along the basal plane i.e c-axis which is perpendicular to the sample normal. This reduction in bond angle yields a comparatively shorter bond length between Mo–O. This shorter bond length can be explained from the knowledge of electronegativity. Electronegativity of O atoms is higher than the S atoms, which leads to a shorter bond length between Mo and O atoms and thus a smaller O–Mo–S bond angle form. Calculated equilibrium bond length between Mo–O using DFT and ReaxFF are in good agreement and their numerical values are 2.072 Å and 2.08 Å respectively, which is comparatively shorter than the equilibrium Mo–S bond length i.e., 2.44 Å [70]. At this point, we are convinced that DFT and ReaxFF outcomes are in good agreement, and we are ready to dope the sample and conduct the simulation using ReaxFF. In our present MD simulations study, at the beginning, we randomly replaced 0.6%, 1.3% and 25% sulfur (S) atoms from 2H–MoS_2 sheet. Afterward, we minimize the model and equilibrate under NPT dynamics for several thousand steps before applying tensile load. Tensile response of the oxygen doped sample alongside pristine sample is shown in Fig. 5c. We do not observe any significant change in mechanical properties at low concentration of doping. For example, mechanical behavior of 0.6% doped sample and pristine samples shows an almost similar trend. This observation indicates that a very low amount of doping or oxidation does not significantly change the mechanical properties of 2H–MoS_2. However, as we increase the doping concentration ultimate failure strain increases at the expense of ultimate failure strength. However, a high amount of doping/oxidation i.e., 25% significantly alters the mechanical properties and both ultimate stress and strength are decreased by a significant amount as shown by deep red color in Fig. 5c. We notice local plastic deformation for all cases of doping. Observed local plastic transformation behavior is very similar to the pristine sample. To investigate the enhancement in plasticity at the expense of strength we have analyzed MD simulation trajectory as shown in Fig. 5d–g. Mulliken atomic population analysis has shown that the O atom has a higher atomic population compared to S atoms in MoS_2 [7], which stimulate stronger Columbic interaction between Mo and O atoms. Thus at higher strain O atom can easily move over Mo atoms and could be trapped between two Mo atoms as shown in Fig. 5d. Thus it forms a virtual vacancy site at its original position which is very similar to V_{s1} type vacancy as indicated by dotted dark color circle in Fig. 5d. This virtual V_{s1} vacancy enhances the plasticity in the sample. Shear strain analysis in Fig. 5e also supports this hypothesis. During straining it is also possible that O atoms could leave their original lattice site and form a new bond with two Mo atoms as shown in Fig. 5f and g. This atomic bond breaking and formation might help to achieve higher plasticity. Due to the O atom doping, we notice a decrement in failure strength by 6.9%, and an increment in failure strain by 12% for 1.3% O atom doped sample. However, as we increase the O doping failure strength reduces significantly and for 25% O doped sample ultimate tensile strength decreased by 8.2% at a tensile strain of 22.4%. Reduction in tensile strength can be explained from Fig. 5h. We notice that even at 9% strain O atoms creates a virtual vacancy at their original lattice position as shown by the dark color dotted circle in Fig. 5h. However, at higher strain due to the excessive O atom doping voids are created and sample fails at 22.4% as shown in Fig. 5i. It can be concluded that O doping and S vacancy has very similar effects on the deformation behavior of MoS_2.

3.3. *Mechanical response of polycrystalline MoS_2*

Synthesis such as large-area chemical vapor deposition (CVD) might yield polycrystalline MoS_2 [71,72]. Temperature also plays an important role in the growth and crystallinity of 2D materials [73,74]. Unlike metals, polycrystalline MoS_2 contains grain boundaries (GBs) with different types of ring 4|6, 4|8, 6|8 and vacancy V_{s1}, $V_{s2,}$ etc. defects [12, 32,75]. These defects could significantly deteriorate the physical properties of 2D materials [76]. Thus in our present study, we have attempted to investigate the effects of grain size and GBs on the mechanical properties of polycrystalline MoS_2. We model 6 different grains size from 3 nm to 15 nm with 3 number of grains as shown in Fig. 6. We implied periodic boundary conditions along all directions to avoid length scale effects. Fig. 6 shows a polycrystalline MoS_2 with 15 nm grains size, and atoms are colored by shear strain. In this study we applied tensile load along X-direction (as shown in Fig. 1a). Similar to the single-crystal sample we notice local plastic deformation originating at the GBs and propagating inside the grain boundary as shown by Fig. 6b (Please see the video 2). This indicates GBs are more vulnerable to the external load. However, unlike single-crystal these local plastic deformation bands are not perpendicular to the loading direction, rather they follow the zigzag edge of the MoS_2. Thus instead of a vertical band, we observe the local plastic deformation band which follows the grain orientation along the zigzag edge as shown in Fig. 6b. This local plastic deformation band continues to grow until it reaches the GB as shown in Fig. 6c and gradually saturates the entire sample. As the local plastic deformation accompanied by S–S bond formation is completed, stress concentration takes place at the GBs as shown in Fig. 6d by pink color dotted box. Due to this stress concentration void forms and gradually grows at the GBs. This void initiates cracking in the sample as shown by Fig. 6f. Inter-granular crack propagates along with the GB until it reaches the triple point, and afterward, we notice *trans*-granular crack propagation as shown in Fig. 6f–h. Unlike single-crystal samples, grains

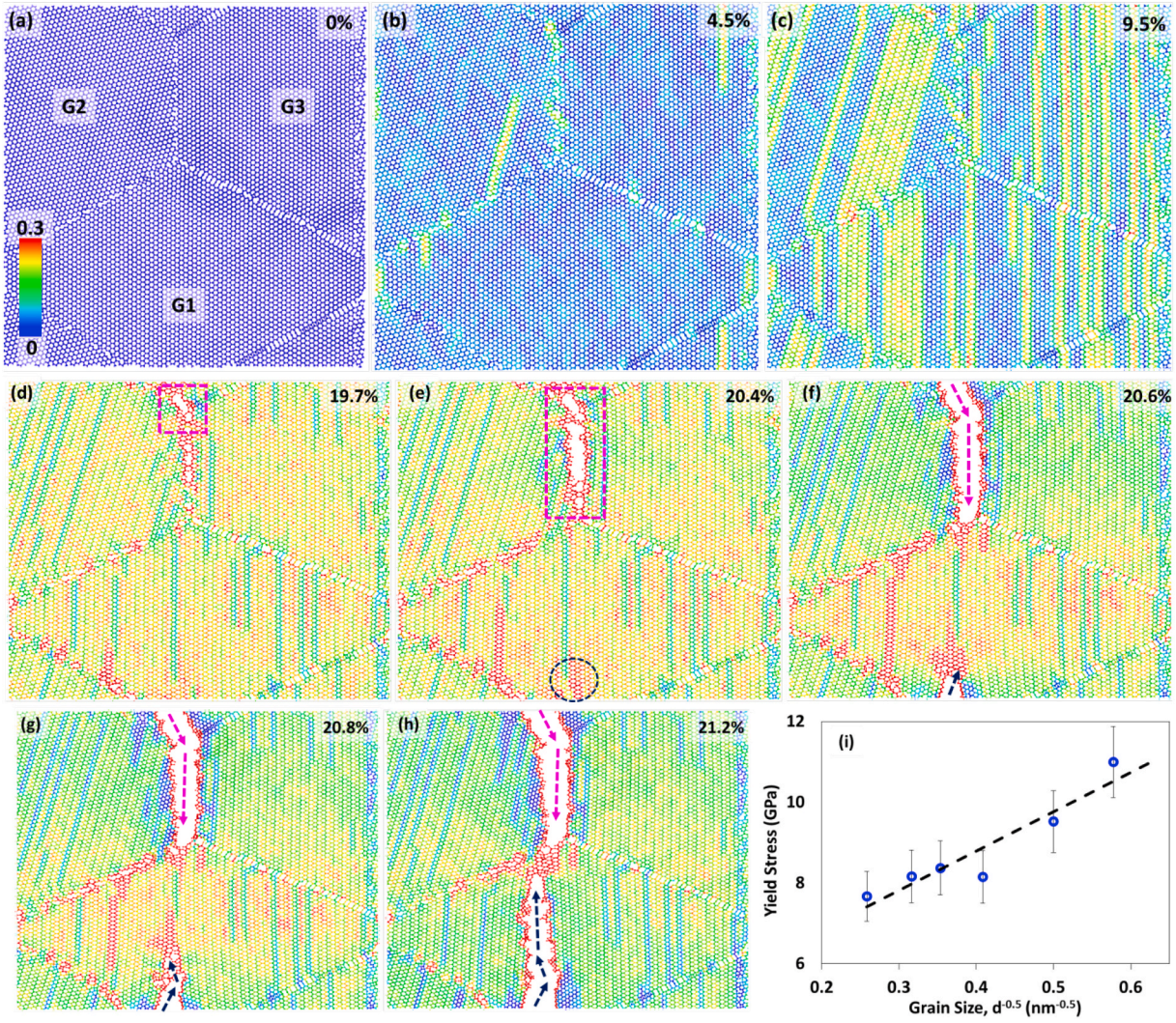

Fig. 6. Tensile response of 2H–MoS_2 at 300 K: (a)–(h) Tensile response of a polycrystalline MoS_2 sample at different strain, and (i) Yield strength and grain size relationship of polycrystalline MoS_2 samples.

are oriented at different angles in a polycrystalline MoS_2 sample. It is noted that in a single crystal sample zigzag edge is the preferred crack propagation direction in MoS_2. Due to this preferred crack propagation direction, we notice crack deflection during crack propagation in a polycrystalline MoS_2 sample. Fig. 6i shows first yield stress variation with grain size and we observed grain boundary strengthening or Hall-Petch effects in polycrystalline MoS_2 sample. GB strengthening effect has been also observed in nanomaterials [77–80]. This effect can be explained from our observed local deformation in a single crystal sample. As the grain size decreases to 3 nm larger amount of force is required to form a local plastic deformation band, and additionally the number of the deformation band also reduces due to the physical size of the individual grain. This reduced grain size resists yielding and contributes to the higher Yield strength as shown in Fig. 6i. On contrary to this, due to the increment in grain size, local plastic deformation can take place at lower external force and it can accommodate more local plastic deformation band which further reduces the Yield strength. Our calculated tensile strength and failure strength of a polycrystalline MoS_2 sample with grain size 15 nm are 15.7 GPa and 20.3%. Lower tensile strength of polycrystalline MoS_2 indicates GBs significantly deteriorates mechanical properties of MoS_2.

3.4. Grain boundary insensitive fracture in MoS_2

To assess the effect of GB orientation angle on mechanical properties of MoS_2, we model polycrystalline MoS_2 sample with different GB angle namely 5°, 10°, 25°, 30°, 45°, and 60° (with respect to the vertical axis as shown in Fig. 7b). To build these GBs structure we rotate two supercell structures with respect to their basal plane i.e., perpendicular to the sample surface as shown in Fig. 7b. Among these six samples, the deformation mechanism for 30° and 45° tilt GBs has been discussed in the following section. Sample with 30° tilt GB contains only 4|8 type ring defects as marked by pink color dotted ring in Fig. 7b. Thus it makes highly ordered GB without introducing any additional adatoms, vacancy or other types of ring (such as 4|6, 6|8, etc.) defects. On contrary to this sample with 45° tilt GB contains different types of ring defects including 4|6, 4|8, vacancy, etc. Fig. 7f and g shows GB and defects. Dark color dotted circle in Fig. 7g indicates 4-ring defects adjacent to four 6-rings. It is obvious that unlike 30° tilt GB, 45° tilt GB does not contain any ordered defects. These random defects at the GB might change the deformation behavior of 45° tilt GB sample compared to 30° tilt GB sample. Fig. 7a shows the comparison of stress-strain response among tilted samples and single-crystal MoS_2 under tensile loading along X-direction (Fig. 7b). We notice that samples with titled GBs have lower failure stress and strain compared to the pristine sample, which indicates GBs no matter what type of defects they contain always deteriorate the

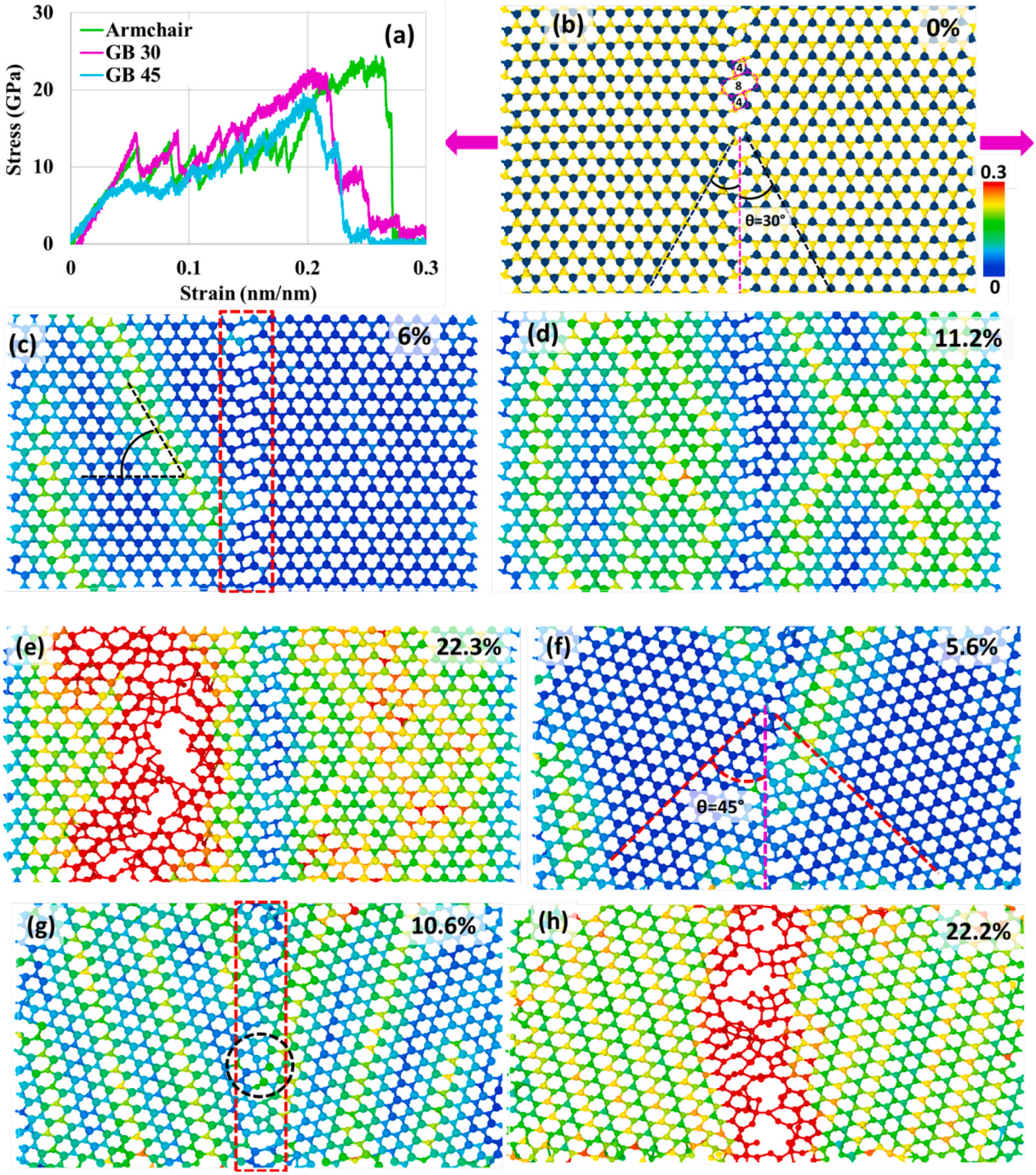

Fig. 7. (a) Tensile response of a polycrystalline MoS_2 sample with tilted GBs at 300 K, (b)–(e) tensile loading and GB insensitive failure of 30° titled sample, and (f)–(h) Deformation behavior of 45° tilted sample (scale bar indicates the magnitude of shear strain in the sample).

physical properties such as strength and fracture toughness. Calculated tensile strength of 30° tilt GB is 21.8 GPa at a failure strain of 21.4%, whereas tensile strength of 45° tilt GB sample is 18.6 GPa at a failure strain of 20.6%. This indicates that ordered GBs such as sample with 30° tilt GB has better performance in terms of mechanical properties compared to the sample containing randomly oriented defects at GBs. During the tensile loading, we also notice local plastic deformation in the tilted GB samples as shown in Fig. 7c and e. For the 30° tilt GB sample, angle between loading direction and plastic deformation band is approximately 60° as shown in Fig. 7c. As we increase the tensile load local plastic deformation band continues to grow and saturates the samples (Fig. 7d). Interestingly, during the failure GBs remains intact as shown in Fig. 7e, which indicates 30° tilt GB sample is insensitive to fracture (Please see the video 3). Insensitivity to fracture can be explained from the 4|8 ring structure. In the previous section, we have shown that crack propagates along the zigzag edge of the sample. However, for 30° tilt GB we do not have any zigzag edge at the GBs as shown in Fig. 7c. Shearing strain at the GBs is also lower compared to the pristine grain interior. Thus stress concentration takes place inside the grain and the sample eventually fails from the interior of the grain as shown in Fig. 7e. Unlike 30° tilt GB sample, the sample with 45° tilt GB has random ring and vacancy defects as shown in Fig. 7f and g. Though local plastic deformation starts inside the grain, however at higher strain stress concentration takes place at the GBs, and thus failure initiates at

the GBs. Besides 30° tilt GB sample, all other types of samples show the similar pattern, which indicates in a polycrystalline MoS_2 sample ordered 4|8 can resist crack propagation. For both samples, we have notice crack deflection along the zigzag edge which also supports zigzag edge as the preferred crack propagation direction in a MoS_2 sample [59,76].

4. Conclusion

In our present study, we investigate mechanical properties of single as well as polycrystalline MoS_2 samples using MD simulations. Our calculated results are in good agreement with the existing literature. Studies show that local plastic deformation in a single-crystal MoS_2 which further introduces serration in tensile response. We also observe grain boundary strengthening i.e., Hall-Petch strengthening in polycrystalline MoS_2 samples. Both tensile response and void nucleation and coalescence at the grain boundaries indicate ductile mode failure in polycrystalline MoS_2 samples. This ductile mode failure in the polycrystalline MoS_2 sample is accompanied by both intra- and *trans*-granular fractures. Alongside polycrystalline sample characterization, we also study individual tilt grain boundary effects on the mechanical response. We notice that grain boundary insensitive fracture in a 30°-tilt grain boundary sample which contains only 4|8 type ring defects. Our study predicts that defects such as vacancy inclusion can enhance ductility at the expense of mechanical strength. We also model oxygen doping in MoS_2 to investigate its effects on mechanical properties. Very similar to S vacancy defects low doping concentration of oxygen atoms in MoS_2 exhibits similar behavior. In all cases i.e., both vacancy and oxygen doping we notice a reduction in Yield strength and strain. In sum, our current findings will provide insights on defects, doping, and GB-based engineering of MoS_2 samples toward the real-world applications in nanoelectronics as well as in nanoelectromechanical systems.

CRediT authorship contribution statement

Zahabul Islam: Conceptualization, Data curation, Formal analysis, Investigation, Methodology, Software, Validation, Visualization, Writing - original draft. **Aman Haque:** Conceptualization, Formal analysis, Funding acquisition, Investigation, Methodology, Project administration, Resources, Supervision, Writing - review & editing.

Declaration of competing interest

The authors declare that they have no known competing financial interests or personal relationships that could have appeared to influence the work reported in this paper.

Acknowledgment

MAH gratefully acknowledges the support from the Division of Civil, Mechanical, & Manufacturing Innovation (Nanomanufacturing program) of the National Science Foundation through award # 1760931. We gratefully acknowledge Professor Adri C.T. van Duin for providing the ReaxFF forcefield.

Appendix A. Supplementary data

Supplementary data to this article can be found online at https://doi.org/10.1016/j.jpcs.2020.109669.

References

[1] H. Kim, W. Kim, M. O'Brien, N. McEvoy, C. Yim, M. Marcia, F. Hauke, A. Hirsch, G. T. Kim, G.S. Duesberg, Optimized single-layer MoS2 field-effect transistors by non-covalent functionalisation, Nanoscale 10 (2018) 17557–17566.
[2] J.S. Kim, J. Kim, J. Zhao, S. Kim, J.H. Lee, Y. Jin, H. Choi, B.H. Moon, J.J. Bae, Y. H. Lee, S.C. Lim, Electrical transport properties of polymorphic MoS2, ACS Nano 10 (2016) 7500–7506.
[3] N.A. Lanzillo, T.P. O'Regan, S.K. Nayak, Band structure modulation in MoS2 multilayers and heterostructures through electric field and strain, Comput. Mater. Sci. 112 (2016) 377–382.
[4] D. Wang, W. Ju, T. Li, Q. Zhou, Z. Gao, Y. Zhang, H. Li, Electronic and magnetic properties of MoS2 monolayers with antisite defects, J. Phys. Chem. Solid. 131 (2019) 119–124.
[5] Y. Miao, H. Bao, W. Fan, F. Ma, Modulation of the electronic structure and magnetism performance of V-doped monolayer MoS2 by strain engineering, J. Phys. Chem. Solid. 142 (2020) 109459.
[6] I.S. Kim, V.K. Sangwan, D. Jariwala, J.D. Wood, S. Park, K.S. Chen, F. Shi, F. Ruiz-Zepeda, A. Ponce, M. Jose-Yacaman, V.P. Dravid, T.J. Marks, M.C. Hersam, L. J. Lauhon, Influence of stoichiometry on the optical and electrical properties of chemical vapor deposition derived MoS2, ACS Nano 8 (2014) 10551–10558.
[7] L.-J. Kong, G.-H. Liu, L. Qiang, Electronic and optical properties of O-doped monolayer MoS2, Comput. Mater. Sci. 111 (2016) 416–423.
[8] M.D. Esrafili, S. Heydari, A promising and new single-atom catalyst for CO oxidation: Si-embedded MoS2 monolayer, J. Phys. Chem. Solid. 135 (2019) 109123.
[9] M.B. Askari, P. Salarizadeh, M. Seifi, S.M. Rozati, Electrocatalytic properties of CoS2/MoS2/rGO as a non-noble dual metal electrocatalyst: the investigation of hydrogen evolution and methanol oxidation, J. Phys. Chem. Solid. 135 (2019) 109103.
[10] S. Bertolazzi, J. Brivio, A. Kis, Stretching and breaking of ultrathin MoS2, ACS Nano 5 (2011) 9703–9709.
[11] Y. Li, P. Chen, C. Zhang, J. Peng, F. Gao, H. Liu, Molecular dynamics simulation on the buckling of single-layer MoS2 sheet with defects under uniaxial compression, Comput. Mater. Sci. 162 (2019) 116–123.
[12] J. Wu, P. Cao, Z. Zhang, F. Ning, S.-s. Zheng, J. He, Z. Zhang, Grain-size-controlled mechanical properties of polycrystalline monolayer MoS2, Nano Lett. 18 (2018) 1543–1552.
[13] U. Yorulmaz, A. Özden, N.K. Perkgöz, F. Ay, C. Sevik, Vibrational and mechanical properties of single layer MXene structures: a first-principles investigation, Nanotechnology 27 (2016) 335702.
[14] B. Radisavljevic, A. Radenovic, J. Brivio, V. Giacometti, A. Kis, Single-layer MoS2 transistors, Nat. Nanotechnol. 6 (2011) 147–150.
[15] V.K. Sangwan, H.N. Arnold, D. Jariwala, T.J. Marks, L.J. Lauhon, M.C. Hersam, Low-frequency electronic noise in single-layer MoS2 transistors, Nano Lett. 13 (2013) 4351–4355.
[16] D.J. Late, B. Liu, H.S. Matte, V.P. Dravid, C.N. Rao, Hysteresis in single-layer MoS2 field effect transistors, ACS Nano 6 (2012) 5635–5641.
[17] H.U. Kim, H.Y. Kim, A. Kulkarni, C. Ahn, Y. Jin, Y. Kim, K.N. Lee, M.H. Lee, T. Kim, A sensitive electrochemical sensor for in vitro detection of parathyroid hormone based on a MoS2-graphene composite, Sci. Rep. 6 (2016) 34587.
[18] A. Smolyanitsky, B.I. Yakobson, T.A. Wassenaar, E. Paulechka, K. Kroenlein, A MoS2-based capacitive displacement sensor for DNA sequencing, ACS Nano 10 (2016) 9009–9016.
[19] Y.J. Park, B.K. Sharma, S.M. Shinde, M.S. Kim, B. Jang, J.H. Kim, J.H. Ahn, All MoS2-based large area, skin-attachable active-matrix tactile sensor, ACS Nano 13 (2019) 3023–3030.
[20] E. Singh, P. Singh, K.S. Kim, G.Y. Yeom, H.S. Nalwa, Flexible molybdenum disulfide (MoS2) atomic layers for wearable electronics and optoelectronics, ACS Appl. Mater. Interfaces 11 (2019) 11061–11105.
[21] M. Amani, R.A. Burke, R.M. Proie, M. Dubey, Flexible integrated circuits and multifunctional electronics based on single atomic layers of MoS2 and graphene, Nanotechnology 26 (2015) 115202.
[22] Y.C. Lin, D.O. Dumcenco, Y.S. Huang, K. Suenaga, Atomic mechanism of the semiconducting-to-metallic phase transition in single-layered MoS2, Nat. Nanotechnol. 9 (2014) 391–396.
[23] Z. Hu, S. Zhang, Y.N. Zhang, D. Wang, H. Zeng, L.M. Liu, Modulating the phase transition between metallic and semiconducting single-layer MoS2 and WS2 through size effects, Phys. Chem. Chem. Phys. : Phys. Chem. Chem. Phys. 17 (2015) 1099–1105.
[24] Y. Jiao, A.M. Hafez, D. Cao, A. Mukhopadhyay, Y. Ma, H. Zhu, Metallic MoS2 for high performance energy storage and energy conversion, Small 14 (2018), e1800640.
[25] Y. Huang, Y. Sun, X. Zheng, T. Aoki, B. Pattengale, J. Huang, X. He, W. Bian, S. Younan, N. Williams, J. Hu, J. Ge, N. Pu, X. Yan, X. Pan, L. Zhang, Y. Wei, J. Gu, Atomically engineering activation sites onto metallic 1T-MoS2 catalysts for enhanced electrochemical hydrogen evolution, Nat. Commun. 10 (2019) 982.
[26] X. Lin, W. Li, Y. Dong, C. Wang, Q. Chen, H. Zhang, Two-dimensional metallic MoS2: a DFT study, Comput. Mater. Sci. 124 (2016) 49–53.
[27] H. Li, J. Wu, Z. Yin, H. Zhang, Preparation and applications of mechanically exfoliated single-layer and multilayer MoS2 and WSe2 nanosheets, Acc. Chem. Res. 47 (2014) 1067–1075.
[28] G.Z. Magda, J. Pető, G. Dobrik, C. Hwang, L.P. Biró, L. Tapasztó, Exfoliation of large-area transition metal chalcogenide single layers, Sci. Rep. 5 (2015) 14714.
[29] X. Wang, H. Feng, Y. Wu, L. Jiao, Controlled synthesis of highly crystalline MoS2 flakes by chemical vapor deposition, J. Am. Chem. Soc. 135 (2013) 5304–5307.
[30] Q. Ji, Y. Zhang, T. Gao, Y. Zhang, D. Ma, M. Liu, Y. Chen, X. Qiao, P.-H. Tan, M. Kan, J. Feng, Q. Sun, Z. Liu, Epitaxial monolayer MoS2 on mica with novel photoluminescence, Nano Lett. 13 (2013) 3870–3877.
[31] Y. Zhan, Z. Liu, S. Najmaei, P.M. Ajayan, J. Lou, Large-area vapor-phase growth and characterization of MoS2 atomic layers on a SiO2 substrate, Small 8 (2012) 966–971.

[32] Z. Islam, K. Zhang, J. Robinson, A. Haque, Quality enhancement of low temperature metal organic chemical vapor deposited MoS2: an experimental and computational investigation, Nanotechnology 30 (2019) 395402.
[33] K.Q. Dang, D.E. Spearot, Effect of point and grain boundary defects on the mechanical behavior of monolayer MoS2 under tension via atomistic simulations, J. Appl. Phys. 116 (2014), 013508.
[34] R. Addou, L. Colombo, R.M. Wallace, Surface defects on natural MoS2, ACS Appl. Mater. Interfaces 7 (2015) 11921–11929.
[35] A.M. van der Zande, P.Y. Huang, D.A. Chenet, T.C. Berkelbach, Y. You, G.-H. Lee, T.F. Heinz, D.R. Reichman, D.A. Muller, J.C. Hone, Grains and grain boundaries in highly crystalline monolayer molybdenum disulphide, Nat. Mater. 12 (2013) 554–561.
[36] Y. Fu, T. Ragab, C. Basaran, The effect of Stone-Wales defects on the mechanical behavior of graphene nano-ribbons, Comput. Mater. Sci. 124 (2016) 142–150.
[37] A. Garg, S.B. Sinnott, Effect of chemical functionalization on the mechanical properties of carbon nanotubes, Chem. Phys. Lett. 295 (1998) 273–278.
[38] M.Z. Islam, M. Mahboob, R.L. Lowe, Mechanical properties of defective carbon nanotube/polyethylene nanocomposites: a molecular dynamics simulation study, Polym. Compos. 37 (2016) 305–314.
[39] M. Hasanian, B. Mortazavi, A. Ostadhossein, T. Rabczuk, A.C.T. van Duin, Hydrogenation and defect formation control the strength and ductility of MoS2 nanosheets: reactive molecular dynamics simulation, Extreme Mech. Lett. 22 (2018) 157–164.
[40] O.V. Yazyev, Y.P. Chen, Polycrystalline graphene and other two-dimensional materials, Nat. Nanotechnol. 9 (2014) 755–767.
[41] Y. Wei, J. Wu, H. Yin, X. Shi, R. Yang, M. Dresselhaus, The nature of strength enhancement and weakening by pentagon–heptagon defects in graphene, Nat. Mater. 11 (2012) 759–763.
[42] Z. Song, V.I. Artyukhov, B.I. Yakobson, Z. Xu, Pseudo Hall–petch strength reduction in polycrystalline graphene, Nano Lett. 13 (2013) 1829–1833.
[43] C. Yi, C. Hu, M. Bai, J. Lv, D. Tang, Molecular dynamics study on the mechanical properties of multilayer MoS2 under different potentials, Nanotechnology 31 (2020) 215703.
[44] S. Xiong, G. Cao, Molecular dynamics simulations of mechanical properties of monolayer MoS2, Nanotechnology 26 (2015) 185705.
[45] B. Mortazavi, A. Ostadhossein, T. Rabczuk, A.C. van Duin, Mechanical response of all-MoS2 single-layer heterostructures: a ReaxFF investigation, Phys. Chem. Chem. Phys. : Phys. Chem. Chem. Phys. 18 (2016) 23695–23701.
[46] J. Jung, H. Bark, D. Byun, C. Lee, D.-H. Cho, Mechanical characterization of phase-changed single-layer MoS 2 sheets, 2D Mater. 6 (2019), 025024.
[47] K.Q. Dang, J.P. Simpson, D.E. Spearot, Phase transformation in monolayer molybdenum disulphide (MoS2) under tension predicted by molecular dynamics simulations, Scripta Mater. 76 (2014) 41–44.
[48] W.L. Spychalski, M. Pisarek, R. Szoszkiewicz, Microscale insight into oxidation of single MoS2 crystals in air, J. Phys. Chem. C 121 (2017) 26027–26033.
[49] S. Kc, R.C. Longo, R.M. Wallace, K. Cho, Surface oxidation energetics and kinetics on MoS2 monolayer, J. Appl. Phys. 117 (2015) 135301.
[50] Q. Yue, S. Chang, S. Qin, J. Li, Functionalization of monolayer MoS2 by substitutional doping: a first-principles study, Phys. Lett. 377 (2013) 1362–1367.
[51] B. Zhao, C. Shang, N. Qi, Z.Y. Chen, Z.Q. Chen, Stability of defects in monolayer MoS2 and their interaction with O2 molecule: a first-principles study, Appl. Surf. Sci. 412 (2017) 385–393.
[52] T. Zhang, A.B. Anderson, Hydrogen oxidation and evolution on platinum electrodes in Base: theoretical study, J. Phys. Chem. C 111 (2007) 8644–8648.
[53] J. Kye, M. Shin, B. Lim, J.-W. Jang, I. Oh, S. Hwang, Platinum monolayer electrocatalyst on gold nanostructures on silicon for photoelectrochemical hydrogen evolution, ACS Nano 7 (2013) 6017–6023.
[54] Y.-R. An, X.-L. Fan, Z.-F. Luo, W.-M. Lau, Nanopolygons of monolayer MS2: best morphology and size for HER catalysis, Nano Lett. 17 (2017) 368–376.
[55] J. Deng, H. Li, J. Xiao, Y. Tu, D. Deng, H. Yang, H. Tian, J. Li, P. Ren, X. Bao, Triggering the electrocatalytic hydrogen evolution activity of the inert two-dimensional MoS2 surface via single-atom metal doping, Energy Environ. Sci. 8 (2015) 1594–1601.
[56] C. Tsai, K. Chan, J.K. Nørskov, F. Abild-Pedersen, Rational design of MoS2 catalysts: tuning the structure and activity via transition metal doping, Catalysis Sci. Technol. 5 (2015) 246–253.
[57] G. Ye, Y. Gong, J. Lin, B. Li, Y. He, S.T. Pantelides, W. Zhou, R. Vajtai, P.M. Ajayan, Defects engineered monolayer MoS2 for improved hydrogen evolution reaction, Nano Lett. 16 (2016) 1097–1103.
[58] T. Chowdhury, J. Kim, E.C. Sadler, C. Li, S.W. Lee, K. Jo, W. Xu, D.H. Gracias, N. V. Drichko, D. Jariwala, T.H. Brintlinger, T. Mueller, H.G. Park, T.J. Kempa, Substrate-directed synthesis of MoS2 nanocrystals with tunable dimensionality and optical properties, Nat. Nanotechnol. 15 (2020) 29–34.
[59] B. Wang, Z. Islam, K. Zhang, K. Wang, J. Robinson, A. Haque, Role of sulphur atoms on stress relaxation and crack propagation in monolayer MoS2, Nanotechnology 28 (2017) 365703.
[60] K. Elibol, T. Susi, M. O'Brien, B.C. Bayer, T.J. Pennycook, N. McEvoy, G. S. Duesberg, J.C. Meyer, J. Kotakoski, Grain boundary-mediated nanopores in molybdenum disulfide grown by chemical vapor deposition, Nanoscale 9 (2017) 1591–1598.
[61] R.C. Cooper, C. Lee, C.A. Marianetti, X.D. Wei, J. Hone, J.W. Kysar, Nonlinear elastic behavior of two-dimensional molybdenum disulfide (vol 87, 035423, 2013), Phys. Rev. B 88 (2013).
[62] S. Plimpton, Fast parallel algorithms for short-range molecular dynamics, J. Comput. Phys. 117 (1995) 1–19.
[63] M.R. Nielsen Oh, Quantum-mechanical theory of stress and force, Phys. Rev. B 32 (1985) 3780–3791.
[64] X. Fan, W.T. Zheng, J.-L. Kuo, D.J. Singh, Structural stability of single-layer MoS2 under large strain, J. Phys. Condens. Matter 27 (2015) 105401.
[65] B. Mortazavi, A. Ostadhossein, T. Rabczuk, A.C.T. van Duin, Mechanical response of all-MoS2 single-layer heterostructures: a ReaxFF investigation, Phys. Chem. Chem. Phys. 18 (2016) 23695–23701.
[66] Z. Islam, B. Wang, K. Hattar, H. Gao, A. Haque, Departing from the mutual exclusiveness of strength and ductility in nanocrystalline metals with vacancy induced plasticity, Scripta Mater. 157 (2018) 39–43.
[67] Y. Pan, Y. Lin, H. Wang, C. Zhang, Vacancy induced brittle-to-ductile transition of Nb5Si3 alloy from first-principles, Mater. Des. 86 (2015) 259–265.
[68] X. Zou, Y. Liu, B.I. Yakobson, Predicting dislocations and grain boundaries in two-dimensional metal-disulfides from the first principles, Nano Lett. 13 (2013) 253–258.
[69] M.D. Segall, P.J.D. Lindan, M.J. Probert, C.J. Pickard, P.J. Hasnip, S.J. Clark, M. C. Payne, First-principles simulation: ideas, illustrations and the CASTEP code, J. Phys. Condens. Matter 14 (2002) 2717–2744.
[70] T. Liang, S.R. Phillpot, S.B. Sinnott, Parametrization of a reactive many-body potential for Mo–S systems, Phys. Rev. B 79 (2009) 245110.
[71] J. Zhang, H. Yu, W. Chen, X. Tian, D. Liu, M. Cheng, G. Xie, W. Yang, R. Yang, X. Bai, D. Shi, G. Zhang, Scalable growth of high-quality polycrystalline MoS2 monolayers on SiO2 with tunable grain sizes, ACS Nano 8 (2014) 6024–6030.
[72] S. Chen, J. Gao, B.M. Srinivasan, G. Zhang, M. Yang, J. Chai, S. Wang, D. Chi, Y.-W. Zhang, Revealing the grain boundary formation mechanism and kinetics during polycrystalline MoS2 growth, ACS Appl. Mater. Interfaces 11 (2019) 46090–46100.
[73] T. Jurca, M.J. Moody, A. Henning, J.D. Emery, B. Wang, J.M. Tan, T.L. Lohr, L. J. Lauhon, T.J. Marks, Low-temperature atomic layer deposition of MoS2 films, Angew. Chem. Int. Ed. 56 (2017) 4991–4995.
[74] R.A. Vilá, R. Rao, C. Muratore, E. Bianco, J.A. Robinson, B. Maruyama, N.R. Glavin, In situ crystallization kinetics of two-dimensional MoS 2, 2D Mater. 5 (2017), 011009.
[75] Z. Islam, A. Kozhakhmetov, J. Robinson, A. Haque, Enhancement of WSe2 FET performance using low-temperature annealing, J. Electron. Mater. 49 (2020) 3770–3779, https://doi.org/10.1007/s11664-020-08087-w.
[76] J. Wu, P. Cao, Z. Zhang, F. Ning, S.S. Zheng, J. He, Z. Zhang, Grain-size-controlled mechanical properties of polycrystalline monolayer MoS2, Nano Lett. 18 (2018) 1543–1552.
[77] N. Hansen, Hall–Petch relation and boundary strengthening, Scripta Mater. 51 (2004) 801–806.
[78] E.O. Hall, The deformation and ageing of mild steel: III discussion of results, in: Proceedings of the Physical Society. Section B, vol. 64, 1951, pp. 747–753.
[79] H. Gleiter, Nanocrystalline materials, in: W.G.J. Bunk (Ed.), Advanced Structural and Functional Materials, Springer Berlin Heidelberg, Berlin, Heidelberg, 1991, pp. 1–37.
[80] C.A. Schuh, T.G. Nieh, Hardness and abrasion resistance of nanocrystalline nickel alloys near the Hall-petch breakdown regime, MRS Proc. 740 (2011). I1.8.